Elsevier Editorial System(tm) for Geochimica et Cosmochimica Acta
Manuscript Draft

Title: Characterization of natural titanomagnetites (Fe3-xTixO4) for studying heterogeneous electron transfer to Tc(VII) in the Hanford subsurface

Article Type: Article

Corresponding Author: Dr Carolyn Isobel Pearce, Ph.D.

Corresponding Author's Institution: Pacific Northwest National Lab

First Author: Carolyn Isobel Pearce, Ph.D.

Order of Authors: Carolyn Isobel Pearce, Ph.D.; Juan Liu; Donald Baer; Odeta Qafoku; Steve Heald; Elke Arenholz; Andrew Grosz; James McKinley; Charles T Resch; Mark Bowden; Mark Engelhard; Kevin Rosso

Abstract: Sediments with basaltic provenance, such as those at the Hanford nuclear reservation, Washington, U.S.A, are rich in Fe-bearing minerals of mixed valence. These minerals are redox reactive with aqueous O_2 or Fe(II), and have the potential to react with important environmental contaminants including Tc. Here, we isolate, identify and characterize natural Fe(II)/Fe(III)-bearing microparticles from Hanford sediments, develop synthetic analogues and investigate their batch redox reactivity with aqueous Tc(VII). Natural Fe-rich mineral samples were isolated by magnetic separation from sediments collected at several locations on Hanford's central plateau. This magnetic mineral fraction was found to represent up to 1 wt% of the total sediment, and be composed of 90% magnetite with minor ilmenite and hematite, as determined by X-ray diffraction. The magnetite contained variable amounts of transition metal impurities consistent with alio- and isovalent metal substitutions for Fe. X-ray microprobe analysis showed that Ti was the most significant impurity, and that these grains could be described with the titanomagnetite formula $Fe_3 xTi_xO_4$, which falls between endmember magnetite (x = 0) and ulvöspinel (x = 1). The dominant composition was determined to be x = 0.15 by chemical analysis and electron probe microanalysis in the bulk, and by L-edge X-ray absorption spectroscopy and X-ray photoelectron spectroscopy at the surface.
Site-level characterization of the titanomagnetites by X-ray magnetic circular dichrosim showed that despite native oxidation, octahedral Fe(II) was detectable within 5 nm of the mineral surface. By testing the effect of contact with oxic Hanford and Ringold groundwaters to reduced Ringold groundwater, it was found that the concentration of this near-surface structural Fe(II) was strongly dependent on aqueous redox condition. This highlights the potential for restoring reducing equivalents and thus reduction capacity to oxidized Fe-mineral surfaces through redox cycling in the natural environment. Reaction of these magnetically-separated natural phases from Hanford sediments with a solution containing 10 ⬚mol. L-1 Tc(VII) showed that they were able to reduce Tc(VII) to Tc(IV) with concurrent oxidation of Fe(II) to Fe(III) at the mineral surface, as were synthetic x = 0.15 microparticle and nanoparticle analogue phases. When differences in the particle surface area to solution volume ratio were taken into consideration, measured Tc(VII) reduction rates for $Fe_3 xTi_xO_4$ (x = 0.15) natural material, synthetic bulk powder and nanoparticles scaled systematically, suggesting possible utility for comprehensive batch and flow reactivity studies.

Cover Letter

Carolyn Pearce
Pacific Northwest National Laboratory
902 Battelle Boulevard
P.O. Box 999, MSIN K8-96
Richland, WA 99352 USA
Tel: 509-371-6380
carolyn.pearce@pnnl.gov

November 2nd 2012

Dear Dr Norman,

Please find attached a manuscript entitled 'Characterization of natural titanomagnetites (Fe$_{3-x}$Ti$_x$O$_4$) for studying heterogeneous electron transfer to Tc(VII) in the Hanford subsurface', submitted for consideration as a regular article to *Geochimica et Cosmochimica Acta*. The authors of the manuscript are as follows:

C. I. Pearce, Pacific Northwest National Laboratory, Richland, WA 99352, USA
 (Corresponding author: MS K8-96, Phone (509)371-6380, E-mail: carolyn.pearce@pnnl.gov)
J. Liu, Pacific Northwest National Laboratory, Richland, WA 99352, USA
D. R. Baer, Pacific Northwest National Laboratory, Richland, WA 99352, USA
O. Qafoku, Pacific Northwest National Laboratory, Richland, WA 99352, USA
S. M. Heald, Argonne National Laboratory, Argonne, IL 60439, USA
E. Arenholz, Advanced Light Source, Lawrence Berkeley National Laboratory, Berkeley, CA 94720, USA
A. E. Grosz, US Geological Survey, Reston, VA, USA
J. P. McKinley, Pacific Northwest National Laboratory, Richland, WA 99352, USA
C.T. Resch, Pacific Northwest National Laboratory, Richland, WA 99352, USA
M. E. Bowden, Pacific Northwest National Laboratory, Richland, WA 99352, USA
M. H. Engelhard, Pacific Northwest National Laboratory, Richland, WA 99352, USA
K. M. Rosso, Pacific Northwest National Laboratory, Richland, WA 99352, USA

All authors have seen the manuscript and agree to its submission to Geochimica et Cosmochimica Acta.

This manuscript describes the isolation and comprehensive characterization of Fe(II)/Fe(III)-bearing microparticles from sediments at the Hanford nuclear reservation, one of the world's most contaminated sites, and the development of synthetic analogues, and the measurement of their electron transfer reactivity with respect to the contaminant Tc(VII). The research focuses on investigating the properties of Hanford subsurface sediments to predict their influence on key chemical processes affecting the stability of radioactive contaminants. More broadly it relates to mechanisms of heterogeneous electron transfer across the mineral-water interface, providing new insights into the importance of Fe(II) in the solid-state and its potential to be recharged by redox interaction with groundwater.

This manuscript is not under review elsewhere, wholly or in part, and will not be while under consideration by GCA.

We would like to suggest the following as Associate Editors who would be appropriate to handle this manuscript:

1) George Helz
2) Jon Chorover
3) Peggy O'Day

We would also like to suggest the following reviewers:

Glenn Waychunas
Geochemistry Department
Lawrence Berkeley National LaboratoryEmail: gawaychunas@lbl.gov
Phone: 510-486-2224

Donald H. Lindsley
Department of Geosciences
Stony Brook Univeristy
E-mail: Donald.Lindsley@sunysb.edu

David J. Wesolowski
Geochemistry and Interfacial Sciences Group
Oak Ridge National Laboratory
Email: wesolowskid@ornl.gov
Phone: (865) 574-6903

Laurent Charlet
CNRS and University of Grenoble, France
Email:charlet38@gmail.com
Phone: +33 (0)4 76 63 51 98

Paul Tratnyek
Department of Environmental and Biomolecular Systems
Oregon Health and Sciences University
Email: tratnyek@ebs.ogi.edu
Phone: 503 748-1023

Thank you very much,

Carolyn Pearce, Ph.D.

Scientist
Geochemistry Group

1   **Characterization of natural titanomagnetites (Fe$_{3-x}$Ti$_x$O$_4$) for studying heterogeneous**

2   **electron transfer to Tc(VII) in the Hanford subsurface**

3

4   C. I. Pearce[1*], J. Liu[1], D. R. Baer[1], O. Qafoku[1], S. M. Heald[2], E. Arenholz[3], A. E. Grosz[4], J. P.

5   McKinley[1], C.T. Resch[1], M. E. Bowden[1], M. H. Engelhard[1] and K. M. Rosso[1]

6

7   [1]Pacific Northwest National Laboratory, Richland, WA 99352, USA

8   [2]Argonne National Laboratory, Argonne, IL 60439, USA

9   [3]Advanced Light Source, Lawrence Berkeley National Laboratory, Berkeley, CA 94720, USA

10   [4]US Geological Survey, Reston, VA, USA

11

12

13

14

15

16

17

18

19

20

21   *Corresponding author: MS K8-96, Phone (509)371-6380

22   E-mail: carolyn.pearce@pnnl.gov

23   **Abstract**

24   Sediments with basaltic provenance, such as those at the Hanford nuclear reservation,

25   Washington, U.S.A, are rich in Fe-bearing minerals of mixed valence. These minerals are redox

26   reactive with aqueous O_2 or Fe(II), and have the potential to react with important environmental

27   contaminants including Tc. Here, we isolate, identify and characterize natural Fe(II)/Fe(III)-

28   bearing microparticles from Hanford sediments, develop synthetic analogues and investigate

29   their batch redox reactivity with aqueous Tc(VII). Natural Fe-rich mineral samples were isolated

30   by magnetic separation from sediments collected at several locations on Hanford's central

31   plateau. This magnetic mineral fraction was found to represent up to 1 wt% of the total sediment,

32   and be composed of 90% magnetite with minor ilmenite and hematite, as determined by X-ray

33   diffraction. The magnetite contained variable amounts of transition metal impurities consistent

34   with alio- and isovalent metal substitutions for Fe. X-ray microprobe analysis showed that Ti

35   was the most significant impurity, and that these grains could be described with the

36   titanomagnetite formula $Fe_{3-x}Ti_xO_4$, which falls between endmember magnetite ($x = 0$) and

37   ulvöspinel ($x = 1$). The dominant composition was determined to be $x = 0.15$ by chemical

38   analysis and electron probe microanalysis in the bulk, and by L-edge X-ray absorption

39   spectroscopy and X-ray photoelectron spectroscopy at the surface.

40   Site-level characterization of the titanomagnetites by X-ray magnetic circular dichrosim

41   showed that despite native oxidation, octahedral Fe(II) was detectable within 5 nm of the mineral

42   surface. By testing the effect of contact with oxic Hanford and Ringold groundwaters to reduced

43   Ringold groundwater, it was found that the concentration of this near-surface structural Fe(II)

44   was strongly dependent on aqueous redox condition. This highlights the potential for restoring

45   reducing equivalents and thus reduction capacity to oxidized Fe-mineral surfaces through redox

46 cycling in the natural environment. Reaction of these magnetically-separated natural phases

47 from Hanford sediments with a solution containing 10 µmol. L^{-1} Tc(VII) showed that they were

48 able to reduce Tc(VII) to Tc(IV) with concurrent oxidation of Fe(II) to Fe(III) at the mineral

49 surface, as were synthetic x = 0.15 microparticle and nanoparticle analogue phases. When

50 differences in the particle surface area to solution volume ratio were taken into consideration,

51 measured Tc(VII) reduction rates for $Fe_{3-x}Ti_xO_4$ ($x = 0.15$) natural material, synthetic bulk

52 powder and nanoparticles scaled systematically, suggesting possible utility for comprehensive

53 batch and flow reactivity studies.

54

55 **Keywords:** Magnetite, titanomagnetite, electron transfer, iron redox cycling, technetium, X-ray

56 diffraction, electron probe microanalysis, X-ray photoelectron spectroscopy, X-ray microprobe,

57 X-ray magnetic circular dichroism

58

1. Introduction

The Hanford site is a former nuclear reprocessing facility occupying 1500 km^2 on the banks of the Columbia River in Washington State, U.S.A. (McKinley et al., 2007). Operations at the site were restricted to specific areas, with nuclear fuel fabrication to the south (300 Area), fuel irradiation to the north (100 Area) and fuel rod processing on the central plateau (200 Area). In the 300 Area, waste fluids and slurries containing U, Al and Cu were stored in process ponds. In the 200 Area, highly-radioactive wastes from Pu production were disposed of in underground tanks. The unintended release of U, Tc and Pu from these storage facilities resulted in contamination of the underlying vadose sediments and the groundwater (McKinley et al., 2007). To predict the distribution and migration potential of these contaminants, it is necessary to understand the geology and mineralogy of the enclosing sediments. To this end, sediment was recovered from boreholes drilled at several locations across the 200 Area on the Central Plateau, and in the 300 Area next to the Columbia River. Table 1 provides details on the geology and the mineralogy of the samples obtained from these locations. The sediments were similar in composition and invariably contained a magnetic, Fe-rich mineral fraction consisting of magnetite, titanomagnetite, ilmenite, Fe(II)/Fe(III) phyllosilicates, and Fe(III) oxides, as well as carbonates, pyroxenes and feldspars, reflecting the underlying basaltic lithology of the Hanford site (Zachara et al., 2007b).

Spinel-type iron oxides such as magnetite (Fe$_3$O$_4$) are key mineral phases at the Hanford site because their structural Fe(II) content is able to affect the form and stability of redox-active contaminants through heterogeneous electron transfer. In the absence of surface passivation, magnetites have been shown to spontaneously reduce and effectively immobilize ^{99}Tc(VII), a major risk-driving contaminant at Hanford, to less soluble Tc(IV) in the form of a mixed Fe(III)-
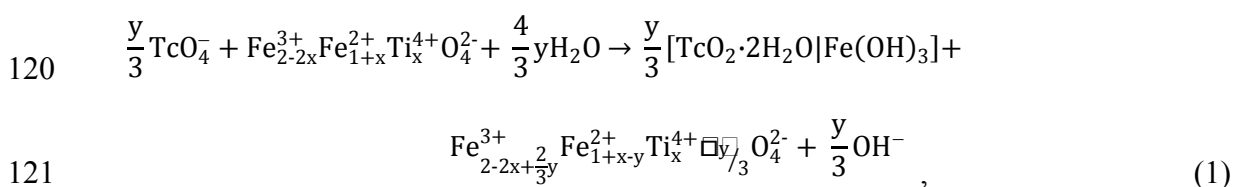
4

82   Tc(IV) co-precipitate (Cui and Eriksen, 1996; Farrell et al., 1999; Ilton et al., 2010; Liu et al.,

83   2012; Skomurski et al., 2011). However, surface passivation is prevalent in oxic aquifer zones as

84   a result of exposure to oxygen from the atmosphere or oxygenated water. The Hanford

85   subsurface also contains reduced zones where there is potential for restoring reducing

86   equivalents to mineral surfaces by exposure to aqueous Fe(II). These oxidation-reduction

87   processes are strongly dependent on the inherent bulk-mineral Fe(II) content and on the Fe(II)

88   distribution and accessibility at the mineral surface.

89   The objective of this study was to obtain fundamental information about the structure and

90   chemical composition of Hanford sediment-derived iron oxides and to assess their potential for

91   electron transfer reactions with contaminants, e.g. Tc(VII), at the oxide-solution interface. To

92   achieve this, natural Fe(II)/Fe(III)-containing mineral samples were isolated by magnetic

93   separation from three sediments collected at two different locations on the Central Plateau of the

94   Hanford site; the Environmental Restoration Disposal Facility (ERDF) and the coarse (SC) and

95   fine (SF) fractions from the Trench 94 Subpit (the excavated site used for storage of scrapped

96   submarine reactor compartments). The magnetic mineral fraction of these sediments was

97   characterized in terms of mineralogy, chemical composition, particle size and morphology, and

98   presence of impurities, by micro-X-ray diffraction (μ-XRD), wet chemical analysis, electron

99   probe microanalysis (EPMA), scanning electron microscopy/energy dispersive spectroscopy

100   (SEM/EDS) and X-ray microprobe/X-ray absorption near edge spectroscopy (XMP/XANES).

101   Due to the importance of the mineral surface when considering the potential for interaction with

102   solution species, the surface composition was examined by *L*-edge X-ray absorption

103   spectroscopy (XAS) and X-ray photoelectron spectroscopy (XPS). The magnetic mineral

104   fraction was also analyzed using X-ray magnetic circular dichroism (XMCD), which is the only

105 technique that allows a clear distinction between possible Fe oxidation states and

106 crystallographic sites at the reactive surface due to the ~4.5 nm (~5 unit cells) probing depth of

107 these measurements in total electron yield mode (Gota et al., 2000).

108   We focused on magnetite-containing Ti(IV) as a major structural substituent, so-called

109 titanomagnetites ($Fe_{3-x}Ti_xO_4$), because this naturally-occurring phase was dominant within the

110 magnetic mineral fraction. Substitution of Fe(III) by Ti(IV) in the lattice yields solid-solution

111 intermediates along the binary join from end-member magnetite (Fe_3O_4, $x = 0$) to ulvöspinel

112 (Fe_2TiO_4, $x = 1$). This substitution is accompanied by reduction of lattice Fe(III) to Fe(II) for

113 charge balance; therefore, a proportional increase in the Fe(II)/Fe(III) ratio to values greater than

114 that in magnetite (1:2) is expected. Because the Ti-content dictates the solid-state Fe(II)/Fe(III)

115 ratio, it also "tunes" the bulk thermodynamic redox potential and thereby controls the rate and

116 extent of electron transfer to contaminant species of interest (Liu et al., 2012).

117   We also examined heterogeneous Tc(VII) reduction by these Hanford titanomagnetites to

118 assess their reducing capacity, a reaction that involves concurrent oxidation of Fe(II) to Fe(III) at

119 the mineral surface. Reduction of Tc(VII) by titanomagnetite could thus be written:

120
$$\frac{y}{3}TcO_4^- + Fe_{2-2x}^{3+}Fe_{1+x}^{2+}Ti_x^{4+}O_4^{2-} + \frac{4}{3}yH_2O \rightarrow \frac{y}{3}[TcO_2 \cdot 2H_2O|Fe(OH)_3] +$$

121
$$Fe_{2-2x+\frac{2}{3}y}^{3+}Fe_{1+x-y}^{2+}Ti_x^{4+}\Box_{y/3}O_4^{2-} + \frac{y}{3}OH^-, \qquad (1)$$

122 yielding titanomaghemite and a relatively insoluble Tc(IV)-Fe(III) phase as expected products,

123 the latter of which is similar to a structurally unspecified mixture of TcO_2 hydrate and

124 ferrihydrite (Liu et al., 2012), consistent with previous work (Lukens et al., 2002; Zachara et al.,

125 2007a). Tc(VII) reduction rates were compared with those obtained for complementary synthetic

126 microparticle and nanoparticle analogue $Fe_{3-x}Ti_xO_4$ phases developed for this comparative

127 purpose. We took advantage of the uniquely well-suited power of XMCD to characterize the

6

128   oxidation state and site occupancy of Fe present at the titanomagnetite surfaces before and after

129   reactivity with Tc(VII), and also before and after exposure to groundwater extracted from

130   different depths in the Hanford subsurface, to determine the potential for oxidation or Fe(II)-

131   recharge of the surface as a result of changes in aqueous redox conditions.

132

133   **2. Experimental Method**

134

135   *2.1 Sediment source and separation*

136   Two operating waste-disposal areas on the Hanford Central Plateau were selected for

137   sediment collection. Five gallons of (i) silty fine sand (SF); (ii) pebbly coarse sand (SC) were

138   collected from the north wall of the trench 94 Subpit (218-E-12B Submarine Burial Ground),

139   12.2 m below ground surface; and five gallons of (iii) interstratified fine, medium and course

140   sands of the Hanford formation (Ice Age flood deposits) of Pleistocene age (15,000-20,000 years

141   old), with occasional finer layers of silty sand were collected from the Environmental

142   Remediation Disposal Facility (ERDF), 12.2 m below ground surface. The sediment separation

143   procedure developed by Baer et al. (2010) was employed to obtain the magnetic mineral fraction.

144   The sediments were (i) dried and riffle split to produce homogeneous sub-splits; (ii) sieved to

145   obtain the -20 mesh (<840 µm) fraction; (iii) elutriated and sonicated to remove the fines; and

146   (iv) passed twice through a free-fall magnetic separation apparatus (Frantz Magnetic Barrier

147   Laboratory Separator LB1) to separate the magnetic mineral fraction.

148

149   *2.2 Micro X-ray diffraction*

150   Crystalline phases in the magnetic mineral fractions (ERDF, SC and SF) were identified

151   using a Rigaku D/Max Rapid II μ-XRD instrument with a 2D image plate detector. X-rays were

152   generated with a MicroMax 007HF generator fitted with a rotating Cr anode ($\lambda = 2.2897$ Å), and

153   focused on the specimen through a 30 μm diameter collimator. μ-XRD patterns were collected

154   for 300 s at 42 kV and 150mA over a 2θ range of 10-150° 2θ Cr Kα1 radiation. Magnetic

155   mineral fraction aliquots were ground dry in an agate mortar and pestle, and loaded into an X-ray

156   amorphous silica capillary (Charles Supper Company, 0.5 mm OD). Samples were diluted with

157   cornstarch (5:1 by volume) to alleviate the problem of reduced intensity, especially at low 2θ,

158   due to the relatively high x-ray absorption of iron oxides. 2DP, Rigaku 2D Data Processing

159   Software (Ver. 1.0, Rigaku, 2007) was used to integrate the diffraction rings captured by the 2-D

160   image plate detector. Analysis of diffraction data was done using JADE 8.5 from Materials Data

161   Inc., and the PDF4+ database from ICSD. The background was fitted by a cubic spline function,

162   and diffraction peaks were fitted using the pseudo-Voigt profile shape function. Quantitative

163   analysis and cell refinement was carried out in JADE using whole pattern fitting with the

164   Reference Intensity Ratio (RIR) reported in the database used to scale the overall intensity of

165   each mineral phase.

166

167   *2.3 Chemical Analysis*

168   The chemical composition of the SF sediment, in terms of Fe(II), and total Fe and Ti was

169   characterized by dissolving in shaken, N_2-sparged 5M HCl inside a glovebox overnight. Fe(II)

170   was determined using the ferrozine method (Stookey, 1970) by adding 0.2 mL of diluted acid

171   digest solution to 1.8 mL ferrozine ($C_{20}H_{15}N_4NaO_7S_2$) reagent (1 g L^{-1} ferrozine in 50 mM

172   HEPES buffer, pH 7.0), and determining aqueous Fe(II) concentration by measuring the

173   absorbance at 562 nm using a Shimadzu UV-2501 PC spectrophotometer. Total Fe and Ti were

174   determined using ICP-MS by adding 0.05 mL of the digested sample to 4.95 mL 2% HNO_3 and

175   measuring on an ICP-MS Agilent 7500.

176

177   *2.4 Electron probe microanalysis*

178   The magnetic mineral fraction from the SF sediment was imbedded in epoxy, wafered

179   using a diamond saw, and prepared as polished100-μm thin sections on fused quartz slides.

180   Samples were carbon coated (HR208 carbon coater, Ted Pella Inc., Redding, CA) prior to

181   analysis. Compositional analyses were done using a JEOL JXA-8200 (JEOL USA, Peabody,

182   MA) electron microprobe operated at an accelerating potential of 20 KeV and a beam current of

183   20 nA, focused on the sample surface (ca. 1μm electron spot size). The instrument was

184   calibrated against commercial mineral and oxide standards (Structure Probe, Inc., West Chester,

185   PA), and data was reduced using a ZAF correction routine (Goldstein et al., 2003).

186

187   *2.5 Scanning electron microscopy/energy dispersive spectroscopy*

188   Particle morphology, surface topography, and the chemical composition of whole

189   particles and polished mounts of the magnetic mineral fraction from the SF sediments was

190   characterized by SEM/EDS. For the particle mount, the sample was placed on carbon tape

191   attached to an aluminium planchette. Whole particle and polished mounts were carbon coated

192   using a vacuum sputtercoater. A JEOL JSM-5900LV SEM equipped with an Oxford INCA EDS

193   system (Oxford Instruments America Inc., Concord, MA), operating in backscattered electron

194   (BSE) emission mode at 20 keV, was used for imaging and qualitative elemental analysis.

195   Particle size and EDS analysis were conducted using automated particle analysis software on a

196 JEOL JXA-8530F electron microprobe equipped with an energy-dispersive X-ray spectrometer

197 at 15 keV. Backscattered electron images were acquired on three randomly selected areas of the

198 sample. All particles that were greater than 5 μm were numbered and analyzed automatically.

199 After size analysis d (~ 1 s), the electron beam was positioned in the center of the particle to

200 collect an EDS spectrum for 30 seconds. Conventional standard ZAF (atomic number, mass

201 absorption and fluorescence) correction was carried out automatically for semi-quantitative EDS

202 analysis.

203

204   *2.6 Synchrotron X-ray microprobe/X-ray absorption near edge spectroscopy*

205   A thin section of the SF magnetic mineral fraction was characterized by XMP and

206 XANES. XMP fluorescence imaging was carried out on beamline 20-ID at the Advanced Photon

207 Source, Argonne National Lab. XMP fluorescence images were collected for Fe, Ti, Mn and V

208 with a beam size of 3 μm x 7.5 μm, and at an energy below the Fe edge (7100 eV) to reduce the

209 Fe signal. A Si (111) monochromator provided an energy resolution of 1 eV at the Fe K edge and

210 0.7 eV at the Ti K edge. X-ray fluorescence images of the thin sections were recorded and used

211 to choose points for subsequent XANES measurements at the Fe and the Ti *K*-edge. Fe and Ti

212 data were taken in fluorescence mode with an Fe foil used for online energy calibration. The

213 XANES data were analyzed using the Athena interface to the IFEFFIT program package (Ravel

214 and Newville, 2005).

215

216   *2.7 X-ray photoelectron spectroscopy*

217   The near-surface composition of the SF magnetic mineral fraction was analyzed by X-ray

218 photoelectron spectroscopy (XPS) to determine the Fe chemical state and to measure the overall

219   particle surface composition. XPS analyses were conducted using a Physical Electronics

220   Quantum 2000 Scanning ESCA Microprobe with a focused monochromatic Al Kα X-ray source

221   (1486.7 eV) source and a spherical section analyzer. Particles were mounted using double-sided

222   plastic tape attached to a Si (100) substrate. Fe 2p photoelectron spectra were compared to

223   reference spectra in Chambers et al. (1998). For large collections of mineral particles, the X-ray

224   beam was operated at approximately 100W power, focused to 100 μm diameter, and rastered

225   over the sample. For the analysis of individual particles, the X-ray beam was focused to ~20 μm

226   to avoid detection of areas away from the particle. Data were collected while using the highly

227   reliable combined electron and ion charge compensation capability that is incorporated on this

228   instrument (Baer et al., 2002; Larson and Kelly, 1998). The spectra were aligned to a carbon

229   peak energy of 284.8 eV (adventitious carbon) which produced highly consistent results for these

230   samples. The compositional results reported in Table S2 for natural and ground surfaces were

231   obtained using standard sensitivity factors in the Phi MultiPak Version 9.1 software package,

232   using peak area intensities after a Shirley background subtraction.

233

234   *2.8 Synchrotron X-ray absorption spectroscopy/X-ray magnetic circular dichroism*

235   A ground sample of the SF magnetic mineral fraction was characterized by XA and

236   XMCD analysis to characterize the mineral surface in terms of Ti content and Fe(II)/Fe(III) ratio.

237   XMCD is the difference in absorption of circularly polarized x rays depending on the relative

238   orientation of magnetization and x ray polarization. XMCD was measured with fixed circular

239   polarization reversing the external magnetic field point by point in an X-ray absorption

240   experiment. XMCD is uniquely sensitive to the oxidation state and local structure of

241   magnetically ordered iron cations near solid surfaces (Chen et al., 1995; Stohr, 1995; van der

11

242 Laan and Thole, 1991; van der Laan et al., 1986). Fe $L_{2,3}$ XA spectra were obtained on beamline

243 4.0.2 at the Advanced Light Source (ALS), Berkeley, CA, using the eight-pole resistive magnet

244 endstation (Arenholz and Prestemon, 2005). Samples were loaded onto carbon tape attached to

245 the sample manipulator in an anoxic N_2 glovebox. XA was monitored in total-electron yield

246 (TEY) mode, which has an effective probing depth of 50 Å (Gota et al., 2000). At each energy

247 point, XA spectra were measured for two opposite magnetization directions by reversing the

248 applied field of 0.6 T. After normalization to incident beam intensity, the XMCD spectrum was

249 obtained as the difference between the two XA spectra (Pattrick et al., 2002). To obtain cation

250 distribution over the two structural Fe site types, the experimental XMCD was fit by means of a

251 nonlinear least-squares analysis, using the calculated spectra for each site. In these calculations,

252 described in van der Laan and Kirkman (1992) and van der Laan and Thole (1991), the 10Dq

253 crystal field parameters were taken as 1.2 and 0.6 eV for Fe *Oh* and *Td* sites. Results were

254 convoluted by a Lorentzian of $\Gamma = 0.3$ (0.5) eV for the L_3 (L_2) edge to account for intrinsic core-

255 hole lifetime broadening and by a Gaussian of $\sigma = 0.2$ eV to account for instrumental

256 broadening. The Ti $L_{2,3}$ XAS was also recorded and was not sensitive to the magnetic field. The

257 Ti/Fe ratio was calculated from the integrated area of the XA spectra for the Fe and Ti $L_{2,3}$-

258 edges taken at the same point on the sample, after background subtraction as described in

259 Droubay (1999).

260

261 *2.9 Effect of aqueous environment on natural titanomagnetite surfaces*
262

263   Groundwater samples were collected over distinct geological strata corresponding to the

264 Hanford formation (12.21 m bgs), the oxidized zone of the Ringold formation (15.90 m bgs) and

265 the reduced zone of the Ringold formation (16.99 m bgs) at the Integrated Field-Scale

266   Subsurface Research Challenge (IFRC) site within the 300 Area of the Hanford Site. Unground

267   'as separated' samples of the SF magnetic mineral fraction (300 mg) were contacted with the

268   groundwater samples (1 mL) in an anoxic N_2 glovebox, with shaking for one week. Samples

269   were dried onto carbon tape, attached to a sample manipulator in an anoxic N_2 glovebox for

270   XA/XMCD measurement. The cation composition of the groundwater samples was determined

271   by HNO_3 acidification followed by ICP-OES. ICP-OES analysis was carried out on a Perkin

272   Elmer Optima 2100 DV ICP-OES with an AS93 auto sampler using a Helix Tracey 4300 DV

273   spray chamber and a SeaSpray nebulizer at 1.5 mL/min flow rate in double distilled 2 % nitric

274   acid (GFS Chemicals, Inc. Cat. 621, lot C141305). Calibrations were made using Ultra

275   Scientific ICP standards (Kingstown, RI) in a dilution range of 0.5 to 3000 ug/L.

276

277   *2.10 Synthesis of titanomagnetite microparticles and nanoparticles (Fe$_{2.85}$Ti$_{0.15}$O$_4$)*

278   Titanomagnetite microparticles of composition consistent with that dominant in the

279   natural samples ($Fe_{2.85}Ti_{0.15}O_4$) were prepared as described in Pearce et al. (2010). A

280   stoichiometric mixture of TiO_2, Fe_2O_3, and Fe metal were ground under acetone, loaded into

281   silver foil and heated at 1170 K in evacuated, sealed quartz tubes for seven days.

282   Titanomagnetite nanoparticles of the same composition were prepared as described in Pearce et

283   al. (2012). A stoichiometric mixture of dissolved $FeCl_2$, $FeCl_3$ and $TiCl_4$ in 0.3M HCl (pH<1)

284   was co-precipitated through the addition of a NH_4OH solution under ambient conditions and in

285   aqueous suspension, in an anoxic N_2 glovebox.

286

287   *2.11 Reactivity studies with Tc(VII)*

288   Glassware and plastic bottles were soaked in 1% HNO_3 overnight and rinsed several

289   times with distilled and deionized water (DDW) before use. Chemicals and plastic equipment

290   were deoxygenated for 24 hours inside an anoxic glovebox prior to use. Reduction experiments

291   were performed in a 97% Ar/3% H_2 atmosphere inside the anoxic glovebox (Thermo, USA)

292   equipped with a palladium catalyst to remove trace O_2. DDW was stored in an anoxic glovebox

293   for preparation of all solutions and suspensions. Chemicals were reagent grade or better. Tc(VII)

294   reduction experiments were conducted in 30 mL glass serum bottles with rubber stoppers and

295   crimp seals. Titanomagnetite was added to HEPES buffer solution, giving a solid : solution ratio

296   of 382 mg : 5 mL for natural materials, 993 mg : 13 mL for microparticles and 1.3 mg : 30 mL

297   for nanoparticles. The bottles were sealed and continuously shaken for 20 hours to allow the

298   titanomagnetites to reach equilibrium with their aqueous environment. A ^{99}Tc(VII) stock solution

299   (5 mM) was prepared by diluting NH_4TcO_4 (Perkin-Elmer Life Science Inc., Boston, MA) in

300   DDW. The bottles were spiked with Tc(VII) solution to give a concentration of 10 µM or 30 µM

301   after the 20 hour equilibration period. The Tc-spiked solutions were continuously shaken and

302   sampled over time. For sampling, aliquots of suspension (1.2 mL) were centrifuged (3000 rpm

303   for 5 mins). The supernatant (1 mL) was mixed with anoxic scintillation cocktail (9 mL) in the

304   glovebox. The sample was counted on a Packard 2500TR liquid scintillation counter (Packard

305   Instrument Co. Meriden, CT) for 10 minutes. Background counts were collected by measuring

306   HEPES buffer solution without Tc(VII). The concentration of Tc(VII) in solution was calculated

307   from the background subtracted counts for the samples in dpm/mL. Control experiments were

308   conducted to test for potential Tc(VII) adsorption onto the glass bottles and the syringe filters.

309

310   **3.   Results and Discussion**

311   *3.1 Characterization of magnetic mineral fraction bulk*

312   Figure 1 shows the Environmental Restoration Disposal Facility (ERDF) and the

313   submarine burial ground trenches, from which bulk sediments were collected in the 200 East

314   Area on the Central Plateau at the Hanford site. Bulk texture and mineralogic compositions of

315   the Hanford formation sediments collected from ERDF and the coarse (SC) and fine (SF)

316   horizons of the trenches, compared with that of Hanford formation sediments collected from the

317   200 West Area Tank Farm on the Central Plateau, and Ringold formation sediments collected

318   from the 300 Area in the Columbia River corridor, are given in Table 1. The mineralogy of the

319   samples was similar, reflecting the basaltic provenance of Hanford site sediments. Based on

320   initial weight of bulk, dry sediment, the magnetic mineral fraction was 1% for SF, 0.5% for

321   EDRF and 0.1% for SC, by weight (Table 1). Representative optical microscopy images of the

322   texture of these fractions, including some authigenic subhedral to euhedral octahedral crystals

323   typical of magnetite, are given in Figure 1. XRD patterns for these SF, ERDF and SC magnetic

324   fractions are shown in Figure S1 and indicate primarily magnetite (~90%) with a smaller

325   quantity of hematite. Sample SF also contained minor ilmenite. A quantitative estimation of the

326   relative abundance of these mineral phases scaled to 100%, ignoring additional remaining trace

327   crystalline or possible undetected amorphous phases, is given in Table 2. The magnetite lattice

328   was consistent for all samples and close to the expected value for pure magnetite (8.396 Å,

329   ICDD 19-629). Due to compositional similarities in the magnetic mineral fraction of these

330   sediments, SF was selected as a representative sample for more detailed subsequent

331   characterization and reactivity experiments, as this sediment contained the highest concentration

332   of magnetic material.

333   Representative EPMA analyses of a thin section of the magnetic mineral fraction of the

334   SF sediment (Table S1) were used to determine chemical composition and assess purity of the

335   mineral phases. Table 3 shows that the mineral phases predominantly consisted of Fe and O, as

336   expected for magnetite. These natural magnetites contained variable amounts of impurities,

337   including Al, Mg, V, Cr, Mn, but with a substantially higher proportion of Ti, consistent with

338   magnetites derived from igneous rocks such as basalt (Cornell and Schwertmann, 2003). That the

339   Ti comprised primarily a structural substituent in the magnetite lattice, as opposed to an

340   interstitial impurity, was an assumption consistent with expectations for typical basalt-derived

341   magnetites (Frost and Lindsley, 1991). The term titanomagnetite applies to magnetite wherein

342   the substitution of Fe(III) by Ti(IV) in the lattice yields formulae conforming to $Fe_{3-x}Ti_xO_4$; a

343   complete solid solution exists along the binary join from magnetite (x = 0) to ulvöspinel (x = 1).

344   Exsolution in intermediate compositions along this binary join for crystallization below the

345   consolute temperature (Lilova et al., 2012), yields coherent intergrowths of Ti-rich and Ti-poor

346   phases (Harrison and Putnis, 1999), as can be seen in the darker lamella around Spot 2 in Figure

347   2A. This phenomenon can also result in formation of very fine-scale microstructures that can

348   only be resolved using TEM (Price, 1980; Smith, 1980). EPMA provided an average

349   composition of grains, but with possible reduced accuracy arising from the likely presence of

350   phase heterogeneity due to fine-scale exsolution in the analysed grains (Goldstein et al., 2003).

351   Nonetheless, the nominal EPMA-based composition of these $Fe_{3-x}Ti_xO_4$ grains, determined by

352   taking an average of all measured Ti/Fe ratios was x = 0.16.

353   Chemical analysis, involving acid digestion, ferrozine assay (for Fe(II) content), and ICP-

354   MS, was carried out on the SF magnetic mineral fraction for a measure of the bulk $Fe_{3-x}Ti_xO_4$

355   composition, in terms of Fe(II), Fe(III) and Ti(IV). The composition was x = 0.17, within error

16

356   of that determined by EPMA. The measured Fe(II)/Fe(III) ratio was 0.663, slightly lower than

357   the theoretical Fe(II)/Fe(III) ratio for x = 0.17 (0.705). The fact that this measured ratio did not

358   exceed the theoretical one was consistent with the identity of these phases as titanomagnetites,

359   i.e., that the Ti was tetravalent and resided in the lattice at cationic sites replacing Fe(III). The

360   slightly lower ratio suggests that these titanomagnetites were slightly oxidized, and thus fell

361   along the binary join between titanomagnetite and titanomaghemite, *c.f.* the titanomaghemite

362   composition on the right hand side of Equation 1.

363   To obtain information on spatial distribution of elements within the SF magnetic mineral

364   fraction, and to assess compositional heterogeneity, polished cross sections were analysed using

365   SEM-EDS (Fig. 2). EDS of the large, homogeneous particle in the center of Figure 2A (Spot 1)

366   showed that this was a relatively pure magnetite particle composed of Fe and O with minor

367   amounts of Mn (Fig. 2B and Table S1). EDS of the particle exhibiting exsolution lamella (Spot

368   2) showed that it contained a significant amount of Ti, corresponding to a composition of

369    $Fe_{2.71}Ti_{0.29}O_4$, with minor impurities of Al, V and Mn (Fig. 2C and Table S1). The darker phase

370   at the edge of the particle (Spot 3) represented a surface coating that was present on some of the

371   particles. EDS shows that it was mostly composed of SiO_2 (Fig. 2D and Table S1).

372   SEM images were also collected for whole particles to give an indication of size and

373   shape. Subhedral to euhedral single crystal octahedra consistent with one dominant habit of

374   magnetite were common; Figure S2 (inset) shows an image of a typical faceted particle. EDS

375   analysis at particle edges, which should emphasize near-surface information, indicated Fe, O and

376   Ti with trace amounts of Mg and Al (Fig. S2 and Table S1). Although the particle in Figure S2

377   was ~200 μm across, size analysis of 102 particles from the SF magnetic mineral fraction

378   indicated that the average mean particle size was 72 μm and the size distribution was relatively

379   narrow with a normal distribution.

380   XMP on thin sections of the magnetic mineral fraction of the SF sediments was carried

381   out on ID20 at the APS to image the distribution of Fe and Ti within individual particles (Fig. 3

382   A, B and C). Sampling points were selected from the images for subsequent XANES

383   measurements to determine the oxidation state of Fe (Fig. 3D) and Ti (Fig. 3E). Figure 3 A and

384   B showed that a significant number of the Fe-containing particles were also Ti rich, consistent

385   with other measurements. Fe K-edge XANES spectra were collected for a particle that was high

386   in both Fe and Ti (Spot 1), a particle that was predominantly Fe with small amounts of Ti (Spot

387   2) and a particle that contained only Fe (Spot 3). The Fe K-edge XANES spectrum for Spot 1

388   showed that the edge was shifted to lower energy than in the reference spectrum for magnetite,

389   and was close to the edge position for reference spectra for titanomagnetite ($Fe_{3-x}Ti_xO_4$, x = 0.9)

390   and ilmenite ($FeTiO_3$), suggesting that this was a more reduced mineral phase containing

391   significantly more Fe(II) than pure magnetite. However, the Spot 1 spectrum did not have a line

392   shape with the characteristic shoulder for titanomagnetite or double peak for ilmenite, so it is

393   possible that this was a mixed phase consistent with fine-scale exsolution lamellae below the

394   resolution of the 3 μm x 7.5 μm focused beam on ID20. The Ti K-edge spectrum in Figure 3E

395   resembled the titanomagnetite spectrum but it is possible that it also included an ilmenite

396   component. The Fe K-edge spectrum for Spot 2 (Fig. 3D) was also shifted to slightly lower

397   energy with respect to the magnetite spectrum and has a low energy shoulder, suggesting that

398   this was a titanomagnetite phase. The Ti K-edge spectrum for Spot 2 (Fig. 3E) was also similar

399   to the reference titanomagnetite spectrum. For Spot 3 (Fig. 3D) the Fe K-edge spectrum was at

400   the same energy as the reference spectrum for magnetite and the line shape was very similar. As

401   this particle only contained Fe, it can be concluded that it was close to end member magnetite.

402   The XMP and XANES data show that, although the SF magnetic mineral fraction was

403   predominantly magnetite according to bulk XRD, on a micron scale, the sample consisted of a

404   range of mineral phases with different compositions. Other potential impurities in the magnetite

405   were also imaged using XMP and the three most significant (Mn, Ti and V) are plotted in terms

406   of their correlation with Fe in Figure S3 A-C. The energy used to collect the XMP fluorescence

407   images (7100 eV) was below the Fe edge to reduce the Fe signal, and it therefore cannot be

408   directly compared to the signal levels of the other elements. However, Figure S3B shows that Ti

409   constituted the impurity present in the highest concentration and had some degree of correlation

410   with the Fe.

411

412   *3.2 Surface characterization*

413   The techniques described thus far emphasize information on the bulk characteristics of

414   the magnetic mineral fraction but, in the environment, it is the mineral surface that interacts with

415   groundwater and contaminants. Two highly surface-sensitive techniques, XPS and XMCD, were

416   employed to determine the composition and potential for reactivity, in terms of the Fe(II)/Fe(III)

417   ratio, at the surface of the SF magnetic mineral fraction. The SEM-EDS results indicated that the

418   surface of some of the particles was covered with an SiO_2-containing coating. To further

419   investigate this coating, XPS was performed out on the 'as separated' material and on material

420   that had been ground in the glovebox under N_2 to expose fresh surfaces. Figure 4 shows high

421   resolution normalized photoelectron spectra of the Fe 2p (Fig. 4A) and O 1s (Fig. 4B) regions at

422   three different analysis areas, referenced to the C 1s line at 284.8 eV. In Figure 4A, the Fe $2p_{3/2}$

423   peak is at 712.3 eV, similar in energy to goethite, suggesting that the surfaces of the 'as

424   separated' particles were oxidized and predominantly composed of Fe(III). After grinding the SF

425   magnetic mineral fraction under N_2 to expose fresh surfaces and limit air oxidation, the Fe $2p_{3/2}$

426   peak was shifted to lower binding energy (711.1 eV), as a result of an increase in the Fe(II)

427   component (Fig. 4A). The shape of the O 1s line also changed after grinding (Fig. 4B). The 'as

428   separated' material had a single peak at 532.0 eV, consistent with the presence of Al_2O_3 and

429   SiO_2, but after grinding a second peak at 530.2 eV was observed, which is consistent with an Fe

430   oxide. Table S2 includes relative atomic concentrations calculated from peak intensities after

431   Shirley background subtraction. The ratios of Fe to Si, Al and O all increased significantly after

432   grinding, consistent with a decrease in the surface coating. The fact that the Fe 2p peak was

433   measurable, even before grinding, suggested that the Al_2O_3/SiO_2-containing surface coating was

434   less than 1-2 nm thick and/or heterogeneous with incomplete surface coverage. Fe thus

435   remained accessible at the surface of these $Fe_{3-x}Ti_xO_4$ phases, with the potential to participate in

436   electron transfer reactions with contaminants in the aqueous environment. The Ti/Fe metal ratios

437   calculated from XPS peak intensities before and after grinding were 0.034 and 0.052

438   respectively. After grinding, the ratio corresponded to a $Fe_{3-x}Ti_xO_4$ composition of x = 0.15,

439   which was in very good agreement with values obtained for the bulk composition from EPMA

440   (x = 0.16) and chemical analysis (x = 0.17). However, the lower Ti/Fe ratio in the 'as separated'

441   material suggested a surface phase that was relatively depleted in Ti and rich in Fe(III), with a

442   bulk composition containing more Ti and more charge-balancing Fe(II)-equivalents consistent

443   with expected stoichiometry in titanomagnetite.

444   To obtain surface-sensitive information on local coordination, bond distances, and

445   magnetic ordering of Fe in the $Fe_{3-x}Ti_xO_4$ structure, samples of the SF magnetic mineral fraction

446   both 'as separated' and after grinding in the glovebox under N_2, were analyzed using XA and

447   XMCD. XA allows the separation of the Fe and the Ti signal to assess their valence states

448   individually. XMCD is sensitive with site-specificity to distinguish magnetic *A*- and *B*-site Fe(II)

449   and Fe(III) in the titanomagnetite structure (inverse spinel), emphasizing that constituency

450   residing within 50 Å of the surface. The background subtracted Fe *L*-edge XA spectrum for the

451   'as separated' SF magnetic mineral fraction had a more intense peak at 709.5 eV, corresponding

452   to Fe(III), whereas the spectrum for the ground sample had lower overall intensity and a more

453   intense peak at 707.8 eV, corresponding to Fe(II) (Fig. 5A) (van Aken et al., 1998). The peak

454   shapes of the background subtracted Ti *L*-edge XA spectra for the samples before and after

455   grinding are very similar, indicating that Ti was tetravalent and in octahedral coordination in

456   both samples (Fig. 5B). However, the intensity of the Ti spectrum was much lower for the 'as

457   separated' sample. The Ti/Fe metal ratios calculated from the integration of the background

458   subtracted spectra before and after grinding were 0.029 and 0.043 respectively (Table 3). This

459   was in agreement with the trend observed in the XPS data that the surface of the 'as separated'

460   particles was depleted with respect to Ti, whereas the fresh surfaces were consistent with the

461   measured bulk stoichiometry. The increased intensity in the low energy peak of the Fe *L*-edge

462   XMCD for the ground sample, corresponding to Fe(II) in octahedral coordination (Fig. 5C)

463   confirmed that the additional Fe(II) was a structural component of the $Fe_{3-x}Ti_xO_4$ phase. The

464   Fe(II)/Fe(III) ratios, calculated from the Fe XMCD experimental spectra (Table 3) increased

465   from 0.37 to 0.69 upon grinding, consistent with the XPS data, showing that the Fe at the surface

466   of the 'as separated' particles was oxidized.

467

468   *3.3 Effect of aqueous environment*

21

469   Despite that fact that the 'as separated' titanomagnetite particles isolated from the SF

470   sediment were coated with a heterogeneous layer of Al_2O_3/SiO_2, Fe was measurable within

471   ~5 nm of the surface both by XPS and XMCD. To determine the extent to which this Fe could

472   participate in electron transfer reactions with species in the aqueous environment, 'as separated'

473   samples of the SF magnetic mineral fraction were contacted for one week with groundwaters

474   from three different depths across a redox boundary in the Hanford subsurface at the 300 Area;

475   the oxic Hanford formation (12.2 m), the oxidized zone of the Ringold formation (15.9 m) and

476   the reduced zone of the Ringold formation (17.0 m). The compositions of the different

477   groundwaters (Table S3) were very similar except that the reduced Ringold sample was slightly

478   more alkaline and contained less nitrate and more nitrite, consistent with more reducing

479   conditions. The surface Fe(II)/Fe(III) ratio of the samples was measured using XMCD to

480   determine if it was affected by the oxygen content of aqueous environment (Fig. S4). The

481   XMCD spectra were normalized to the intensity of the Fe(III) tetrahedral site for relative

482   comparison and the inset in Figure S4 shows that octahedral Fe(II) peak intensity changes in

483   response to different groundwaters. The octahedral Fe(II) peak increased slightly upon exposure

484   to the oxic Hanford and Ringold groundwater, as compared to the initial 'as separated' material.

485   This was expected as the 'as separated' material was stored in air, 21% oxygen by volume,

486   whereas air-saturated water contains 8.22 mg L^{-1} oxygen at room temperature. As expected, the

487   Fe(II)/Fe(III) ratios for the samples contacted with the two oxic groundwaters were very similar

488   (0.42 and 0.43 for Hanford and oxidized Ringold respectively). A more significant increase in

489   octahedral Fe(II) was observed upon contact with the reduced Ringold groundwater. The Fe site

490   occupancies and Fe(II)/Fe(III) ratios for the samples are given in Table 3, showing that the

491   Fe(II)/Fe(III) ratio had increased from 0.37 for the 'as separated' sample to 0.49 after contact

492   with the reduced Ringold groundwater. Although the increase did not fully restore the

493   Fe(II)/Fe(III) ratio to that found for samples exposing fresh surfaces by grinding (0.69), the shift

494   was significant and in the expected direction. These results showed that structural Fe at the

495   mineral-solution interface was highly responsive to changes in the aqueous environment, and, if

496   initially oxidized, could be reduced to electron donating Fe(II) by transition of the aqueous

497   environment from oxidizing to reducing. In principle, this structural Fe(II) was then capable of

498   catalysing the reduction of polyvalent contaminant species such as ^{99}Tc(VII) in the groundwater

499   by heterogeneous electron transfer at the mineral-solution interface.

500
501   *3.4 Pertechnetate reactivity studies*

502   Batch reactivity studies were conducted to measure the extent and rate of Tc(VII) reduction

503   by the natural titanomagnetite particles. To provide sufficient reactive surface area to observe a

504   reaction on accessible laboratory time scales, SF magnetic mineral was ground under N_2. The

505   results in Figure 6 A show that the exposed surfaces of these titanomagnetites were reactive with

506   respect to the reduction of Tc(VII) to Tc(IV), as indicated by a progressive decrease in Tc(VII)

507   in solution using LSC, compared with a control that contained no mineral phase. Samples of the

508   natural titanomagnetite particles before and after reaction for 114 days were analyzed using

509   XMCD, which confirmed that reduction of Tc(VII) to Tc(IV) occurred with concurrent oxidation

510   of Fe(II) to Fe(III) at the mineral surface, *c.f.*, Equation 1. The decrease in intensity of the peak

511   corresponding to Fe(II) in octahedral coordination in the XMCD spectrum after reaction (Fig. 6

512   B) showed that reduction of Tc(VII) resulted in a measurable decrease in surface Fe(II)/Fe(III)

513   ratio from 0.69 before reaction to 0.63 after reaction.

514   To approximate the redox reactivity of natural titanomagnetites with respect to groundwater

515   contaminants such as Tc(VII) more comprehensively as a function of Ti content, surface

516   composition, and degree of pre-oxidation, and to characterize the products of reduction, it was

517   necessary to generate synthetic analogue mineral phases. Taking an average of the values

518   obtained from all of the characterization techniques for the SF magnetic mineral fraction, for

519   bulk (EPMA and chemical analysis) and surface (XPS and XAS), the general formula for this

520   natural material on average was $Fe_{2.85}Ti_{0.15}O_4$. Synthetic titanomagnetite nanoparticulate

521   materials of the same composition (x = 0.15) were thus prepared using an aqueous-based,

522   ambient temperature synthesis to provide high surface area pristine material compatible with

523   batch reactivity studies (Pearce et al., 2012). To provide an intermediate-length-scale material

524   between the high surface area nanomaterials and the coarse natural materials, micron-sized

525   x = 0.15 titanomagnetites were also prepared using a high temperature synthesis route (Pearce et

526   al., 2010). To link reaction rates observed using nanoparticles, microparticles, and natural

527   materials, the influence of surface area on reactivity with Tc(VII) must be included. SEM images

528   of natural particles (Fig. S5 A), synthetic microparticles (Fig. S5 B) and synthetic nanoparticles

529   (Fig. S5 C) illustrate differences in particles size and surface area between the samples. A

530   summary of the characteristics of the different titanomagnetite particles determined from

531   previous work is given in Table 4. When differences in experimental conditions, specifically

532   particle surface area to solution volume ratio, are taken into consideration as described in Cui

533   and Eriksen (1996), the measured reduction rate for natural particles ($0.032\mu M\ day^{-1}$) was found

534   to be slower than that for microparticles ($0.38\mu M\ day^{-1}$), which in turn was found to be slower

535   than that for nanoparticles ($2.868\ \mu M\ day^{-1}$). While this suggested nonlinearity in the relationship

536   between particle size and reduction rate, the effect appeared constant and predictable by length

537   scale. The effect may arise from coupling of outermost surface electron transfer reactivity to a

538   sustaining resupply of reducing equivalents from the underlying near-surface region, a process

539   that may require simultaneous solid-state diffusion of $e–$ and Fe(III) (Pearce et al., 2012),

540   becoming disproportionately more efficient with decreasing particle size. *K*-edge XA

541   spectroscopy was used to determine the Tc oxidation state and bonding environment in the

542   reacted titanomagnetite x=0.15 nanoparticles (Liu et al., 2012). The line shape of the XANES

543   spectra was consistent with a Tc oxidation state of 4+. The radial transforms of the Tc-EXAFS

544   data for the Tc(IV) precipitate on the $Fe_{2.85}Ti_{0.15}O_4$ nanoparticle samples was modeled with a

545     $TcO_2 \cdot nH_2O$ linear chain developed by Lukens et al. (2002), which was extended to include edge

546   sharing octahedral interactions with an Fe–O surface in Zachara et al. (2007a). It consists of

547   variable length edge-sharing chains of Tc–O octahedra at R = 1.99Å bonded in an edge-sharing

548   fashion to Fe–O octahedra located on the surface of the host Fe(III) oxide substrate (LIU et al.,

549   2012).

550

551   **4. Conclusions**

552   Hanford sediments contain a magnetic mineral fraction (~2 wt%) composed of 90%

553   titanomagnetite ($Fe_{3-x}Ti_xO_4$; where x~0.15). Solid-phase Fe(II), measurable within 5 nm of the

554   mineral surface using *L*-edge XAS and XPS, was highly responsive to changes in the aqueous

555   environment, such as exposure to 300 area groundwater taken above and below the redox

556   boundary. Reaction with a 10 μM Tc(VII) solution showed that natural magnetic isolates

557   reduced Tc(VII) with concurrent oxidation of Fe(II) to Fe(III) at the mineral surface, as did

558   compositionally pristine synthetic microparticle and nanoparticle analogue phases. When particle

559   surface area to solution volume ratio was taken into consideration, Tc(VII) reduction rates for

560   natural particles and synthetic microparticles and nanoparticles could be predicted by a scaling

561   relationship, supporting utility of the synthetic nanoparticles and microparticles for batch and

562 flow reactivity studies to comprehensively studies of titanomagnetite reactivity in environmental

563 systems such as the Hanford site.

564

576

577 **References**

578

579 Ames, L.L., 1974. Characterization of acitnide bearing soils: Top sixty centimeters of 216-Z-9
580   enclosed trench. Pacific Norwest Naional Laboratory, Richland, Washington.
581 Arenholz, E., Prestemon, S.O., 2005. Design and performance of an eight-pole resistive magnet
582   for soft x-ray magnetic dichroism measurements. Rev. Sci. Instrum. 76, 083908.
583 Baer, D.R., Engelhard, M.H., Gaspar, D.J., Lea, A.S., Windisch, C.F., 2002. Use and limitations
584   of electron flood gun control of surface potential during XPS: Two non-homogeneous sample
585   types. Surf. Interface Anal. 33, 781-790.
586 Baer, D.R., Grosz, A.E., Ilton, E.S., Krupka, K.M., Liu, J., Penn, R.L., Pepin, A., 2010.
587   Separation, characterization and initial reaction studies of magnetite particles from Hanford
588   sediments. Phys. Chem. Earth 35, 233-241.
589 Chambers, S.A., Kim, Y.J., Gao, Y., 1998. Fe $2p$ core-level spectra for pure, epitaxial α-
590     $Fe_2O_3(0001)$, γ-$Fe_2O_3(001)$, and $Fe_3O_4(001)$. Surf. Sci. Spectra 5, 219.

591   Chen, C.T., Idzerda, Y.U., Lin, H.J., Smith, N.V., Meigs, G., Chaban, E., Ho, G.H., Pellegrin, E.,
592   Sette, F., 1995. Experimental confirmation of the X-ray magnetic circular dichroism, sum-
593   rules for iron and cobalt. Phys. Rev. Lett. 75, 152-155.
594   Cornell, R.M., Schwertmann, U., 2003. The Iron Oxides: Structure, Properties, Reactions,
595   Occurence, and Uses. Weinheim: Wiley-VCH, New York, New York.
596   Cui, D.Q., Eriksen, T.E., 1996. Reduction of pertechnetate in solution by heterogeneous electron
597   transfer from Fe(II)-containing geological material. Environ. Sci. Technol. 30, 2263-2269.
598   Droubay, T.C., 1999. Soft x-ray spectroscopy and microspectroscopy of magnetic and naturally
599   occurring materials. University of Wisconsin-Milwaukee, Milwaukee, Wisconsin.
600   Farrell, J., Bostick, W.D., Jarabek, R.J., Fiedor, J.N., 1999. Electrosorption and reduction of
601   pertechnetate by anodically polarized magnetite. Environ. Sci. Technol. 33, 1244-1249.
602   Frost, B.R., Lindsley, D.H., 1991. Occurence of iron-titanium oxides in igneous rocks, in:
603   Lindsley, D.H. (Ed.), Oxide Minerals: Petrological and Magnetic Significance. Mineralogical
604   Society of America, Chantilly, Virginia.
605   Goldstein, J.I., Newberry, D.E., Joy, D.C., Lyman, C.E., Echlin, P., Lifshin, E., Sawyer, L.,
606   Michael, J., 2003. Scanning Electron Microscopy and X-Ray Microanalysis, 3rd ed.
607   Springer, New York, New York.
608   Gota, S., Gautier-Soyer, M., Sacchi, M., 2000. Fe $2p$ absorption in magnetic oxides: Quantifying
609   angular-dependent saturation effects. Phys. Rev. B 62, 4187–4190.
610   Harrison, R.J., Putnis, A., 1999. The magnetic properties and crystal chemistry of oxide spinel
611   solid solutions. Surv. Geophys. 19, 461-520.
612   Ilton, E.S., Boily, J.-F., Buck, E.C., Skomurski, F.N., Rosso, K.M., Cahill, C.L., Bargar, J.R.,
613   Felmy, A.R., 2010. Influence of dynamical conditions on the reduction of U^{VI} at the
614   magnetite−solution interface. Environ. Sci. Technol. 44, 170–176.
615   Larson, P.E., Kelly, M.A., 1998. Surface charge neutralization of insulating samples in x-ray
616   photoemission spectroscopy. J. Vac. Sci. Technol. A 16, 3483-3489.
617   Lilova, K.I., Pearce, C.I., Gorski, C.A., Rosso, K.M., Navrotsky, A., 2012. Thermodynamics of
618   the magnetite-ulvöspinel (Fe_3O_4-Fe_2TiO_4) solid solution. Am. Mineral. In press.
619   Liu, J., Pearce, C.I., Qafoku, O., Arenholz, E., Heald, S.M., Rosso, K.M., 2012. Tc(VII)
620   reduction kinetics by titanomagnetite ($Fe_{3-x}Ti_xO_4$) nanoparticles. Geochim. Cosmochim. Ac.
621   96, 67-81.
622   Lukens, W.W., Bucher, J.J., Edelstein, N.M., Shuh, D.K., 2002. Products of pertechnetate
623   radiolysis in highly alkaline solution: structure of $TcO_2 \cdot H_2O$. Environ. Sci. Technol. 36,
624   1124-1129.
625   McKinley, J.P., Zachara, J.M., Wan, J., McCready, D.E., Heald, S.M., 2007. Geochemical
626   controls on contaminant uranium in vadose Hanford formation sediments at the 200 Area and
627   300 Area, Hanford Site, Washington. Vadose Zone J. 6, 1004-1017.
628   Pattrick, R.A.D., van der Laan, G., Henderson, C.M.B., Kuiper, P., Dudzik, E., Vaughan, D.J.,
629   2002. Cation site occupancy in spinel ferrites studied by x-ray magnetic circular dichroism:
630   developing a method for mineralogists. Eur. J. Mineral. 14, 1095-1102.
631   Pearce, C.I., Henderson, C.M.B., Telling, N.D., Pattrick, R.A.D., Charnock, J.M., Coker, V.S.,
632   Arenholz, E., Tuna, F., van der Laan, G., 2010. Fe site occupancy in magnetite-ulvöspinel
633   solid solutions: A new approach using x-ray magnetic circular dichroism. Am. Mineral. 95,
634   425-439.
635   Pearce, C.I., Qafoku, O., Liu, J., Arenholz, E., Heald, S.M., Kukkadapu, R.K., Gorski, C.A.,
636   Henderson, C.M.B., Rosso, K.M., 2012. Synthesis and properties of titanomagnetite (Fe_3-

637 $_x$Ti$_x$O$_4$) nanoparticles: A tunable solid state Fe(II/III) redox system. J. Colloid. Interf. Sci.,
638   387, 24-38.
639 Peretyazhko, T.S., Zachara, J.M., Kukkadapu, R.K., Heald, S.M., Kutnyakov, I.V., Resch, C.T.,
640   Arey, B.W., Wang, C.M., Kovarik, L., Phillips, J.L., Moore, D.A., 2012. Pertechnetate
641   (TcO$_4^-$) reduction by reactive ferrous iron forms in naturally anoxic, redox transition zone
642   sediments from the Hanford Site, USA. Geochim. Cosmochim. Ac., 92, 48-66.
643 Price, G.D., 1980. Exsolution microstructures in titanomagnetites and their magnetic
644   significance. Phys. Earth Planet. In. 23, 2-12.
645 Ravel, B., Newville, M., 2005. ATHENA, ARTEMIS, HEPHAESTUS; Data analysis for x-ray
646   absorption spectroscopy using IFEFFIT. J. Synchrotron Radiat. 12, 537–541.
647 Skomurski, F.N., Ilton, E.S., Engelhard, M.H., Arey, B.W., Rosso, K.M., 2011. Heterogeneous
648   reduction of U^{6+} by structural Fe^{2+} from theory and experiment. Geochim. Cosmochim. Ac.
649   75, 7277-7290.
650 Smith, P.P.K., 1980. Spinodal decomposition in titanomagnetite. Am. Mineral. 65, 1038-1043.
651 Stohr, J., 1995. X-ray magnetic circular dichroism spectroscopy of transition metal thin films. J.
652   Electron Spectrosc. 75, 253-272.
653 Stookey, L.L., 1970. Ferrozine - A new spectrophotometric reagent for iron. Anal. Chem. 42,
654   779.
655 van Aken, P.A., Liebscher, B., Styrsa, V.J., 1998. Quantitative determination of iron oxidation
656   states in minerals using Fe L$_{2,3}$-edge electron energy-loss near-edge structure spectroscopy.
657   Phys. Chem. Miner. 25, 323-327.
658 van der Laan, G., Kirkman, I.W., 1992. The 2p absorption-spectra of 3d transition-metal
659   compounds in tetrahedral and octahedral symmetry. J. Phys-Condens. Mat. 4, 4189-4204.
660 van der Laan, G., Thole, B.T., 1991. Strong magnetic-x-ray dichroism in 2p absorption-spectra
661   of 3d transition-metal ions. Phys. Rev. B 43, 13401-13411.
662 van der Laan, G., Zaanen, J., Sawatzky, G.A., Karnatak, R.C., Esteva, J.M., 1986. Comparison
663   of x-ray absorption with x-ray photoemission of nickel dihalides and NiO. Phys. Rev. B 33,
664   4253-4263.
665 Zachara, J.M., Heald, S.M., Jeon, B.H., Kukkadapu, R.K., Liu, C.X., McKinley, J.P.,
666   Dohnalkova, A.C., Moore, D.A., 2007a. Reduction of pertechnetate [Tc(VII)] by aqueous
667   Fe(II) and the nature of solid phase redox products. Geochim. Cosmochim. Ac. 71, 2137-
668   2157.
669 Zachara, J.M., Serne, J., Freshley, M., Mann, F., Anderson, F., Wood, M., Jones, T., Myers, D.,
670   2007b. Geochemical processes controlling migration of tank wastes in Hanford's vadose
671   zone. Vadose Zone J. 6, 985-1003.
672
673

674

Figure legends

676

677 **Figure 1.** Source and texture of magnetic mineral fractions isolated from sediments at the

678 submarine burial ground and the Environmental Restoration Disposal Facility at the Hanford

679 site, Washington, U.S.A.

680

681 **Figure 2.** SEM images of particles from the SF magnetic mineral fraction in polished cross

682 section (A), showing EDS analysis from a magnetite-rich area (Spot 1, B), a titanomagnetite-rich

683 area (Spot 2, C) and the surface coating (Spot 3, D).

684

685 **Figure 3.** X-ray fluorescence microprobe analyses of the SF magnetic mineral fraction showing

686 Fe (A), Ti (B) and Fe-Ti (C) distribution, although with Fe K-edge (D) and Ti K-edge (E)

687 XANES spectra for different points on the XMP map, along with magnetite, titanomagnetite and

688 ilmenite reference spectra.

689

690 **Figure 4.** High resolution photoelectron spectra of the Fe 2p region (A) and the O 1s region (B)

691 for three different analysis areas on the 'as separated' SF magnetic mineral fraction (grey lines)

692 and on N_2-ground SF magnetic mineral fraction (black lines).

693

694 **Figure 5.** XA spectra at the Fe L-edge (A) and the Ti L-edge (B), along with Fe L-edge XMCD

695 difference spectra (C) for the 'as separated' SF magnetic mineral fraction (black lines) and on

696 N_2-ground SF magnetic mineral fraction (red lines).

697

698

699   **Figure 6.** Reduction in Tc(VII) concentration with time (A) for the control (black line) and after

700   exposure to the N_2-ground SF magnetic mineral fraction (red line) with corresponding Fe *L*-edge

701   XMCD difference spectra (B), before (black line) and after (red line) Tc(VII) reduction.

702

703

704

Table 1: Analyses of sediments from the Hanford Site

Sample Site	Geology	Mineralogy	Reference
Environmental Restoration Disposal Facility (ERDF)	Interstratified fine, medium and course sands of the Hanford formation (Ice Age flood deposits) of Pleistocene age (15-20 K years old). Occasional finer layers of silty sand ranging to sandy silt slackwater deposits.	Feldspar, quartz, 0.5 wt. % magnetite	This work
200 East Area: Trench 94 Subpit (218-E-12B Burial Ground) - silty, fine sand (SF)	Silty, fine sand from 12.2 m below ground surface (bgs). 3 m above bedrock.	Feldspar, quartz, 1 wt. % magnetite	This work
200 East Area: Trench 94 Subpit (218-E-12B Burial Ground) - pebbly sand (SC)	Pebbly sand from 12.2 m bgs. 3 m above bedrock.	Feldspar, quartz, 0.1 wt. % magnetite	This work
200 West Area: Trench Z-9 (Plutonium Finishing Plant Complex)	Sandy silt from 29 m bgs.	Quartz, magnetite, ilmenite, Clay: kaolinte, illite Feldspar: orthoclase Ilmenite Mica: biotite, muscovite	(Ames, 1974)
200 West Area: Borehole 299-W22-50 (South East corner of S-SX Tank Farm)	Fine-grained silty sediments (<2 mm) of the Hanford formation from 66-72 m bgs, just above water table.	43.0 wt.% quartz, 30.0 wt.% plagioclase, 7.4 wt.% orthoclase, 4.5 wt.% mica, 2.0 wt.% amphibole, 1.0 wt.% chlorite, 0.1 wt.% magnetite	(Baer et al., 2010; McKinley et al., 2007)
300 Area: 55m borehole (South Processing Pond)	Pliocene-age Ringold formation at 51.5-51.8 m bgs consisting of fine-grained deposits. Basalt bedrock exists below Ringold Formation at ~58 m bgs.	Quartz, cristobalite, feldspar, calcite, hematite, magnetite; traces of smectite	(Peretyazhko et al., 2012)

706

707

708 **Table 2:** Quantitative estimation of mineral phases present in magnetic mineral fractions isolated

709 from Hanford sediments

Sample	Estimated fractions		Magnetite cell /Å	Other phases
	Magnetite	**Hematite**		
SC	92%	8%	8.3981(13)	
ERDF	93%	7%	8.3968(11)	
SF	80%	11%	8.3955(12)	Ilmenite (10%)

710

711

712 **Table 3.** Site occupancies from XMCD for SF magnetic mineral fraction

Sample	$Fe^{2+}\,d^6O_h$	$Fe^{3+}\,d^5T_d$	$Fe^{3+}\,d^5O_h$	Fe(II)/Fe(III)	Ti/Fe
Unground	0.77	0.95	1.13	0.37	0.029
Ground	1.16	0.87	0.81	0.69	0.043
Hanford	0.84	0.98	1.02	0.42	0.022
Ringold Oxidized	0.85	0.95	1.05	0.43	0.017
Ringold Reduced	0.94	0.92	1.00	0.49	0.015
Ground (after Tc(VII) exposure)	1.1	0.89	0.86	0.63	-

713

714

715   **Table 4.** Characteristics of natural and synthetic titanomagnetite reactivity

Material	Size µm	Cell parameter Å	solid/solution m/V g/cm^3	rate of TcO$_4^-$ reduction µM day^{-1}
Natural particles	72.0	8.3940	0.000888	0.0315
Microparticles	8.2	8.4161	0.00932	0.380
Nanoparticles	0.0094	8.4155	0.00461	2.868

716
717
718
719

Figure 1
Click here to download high resolution image
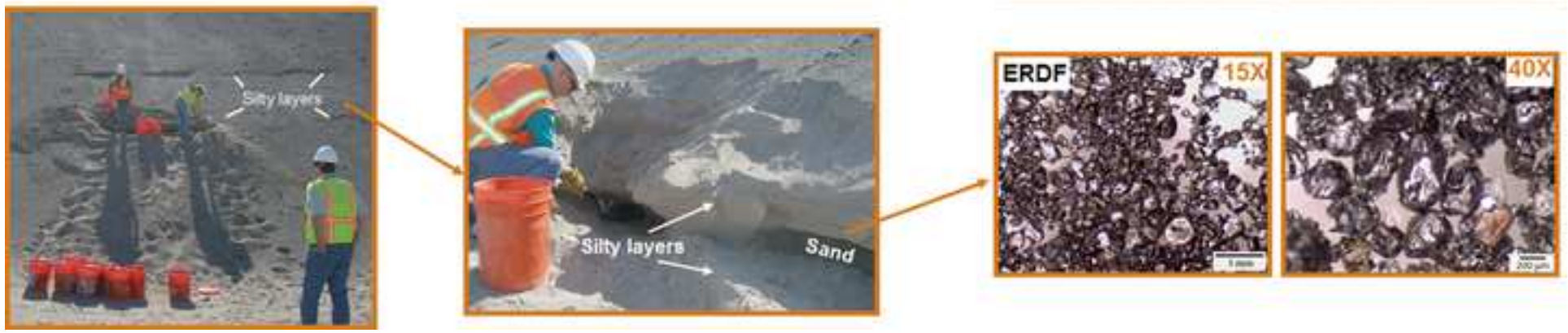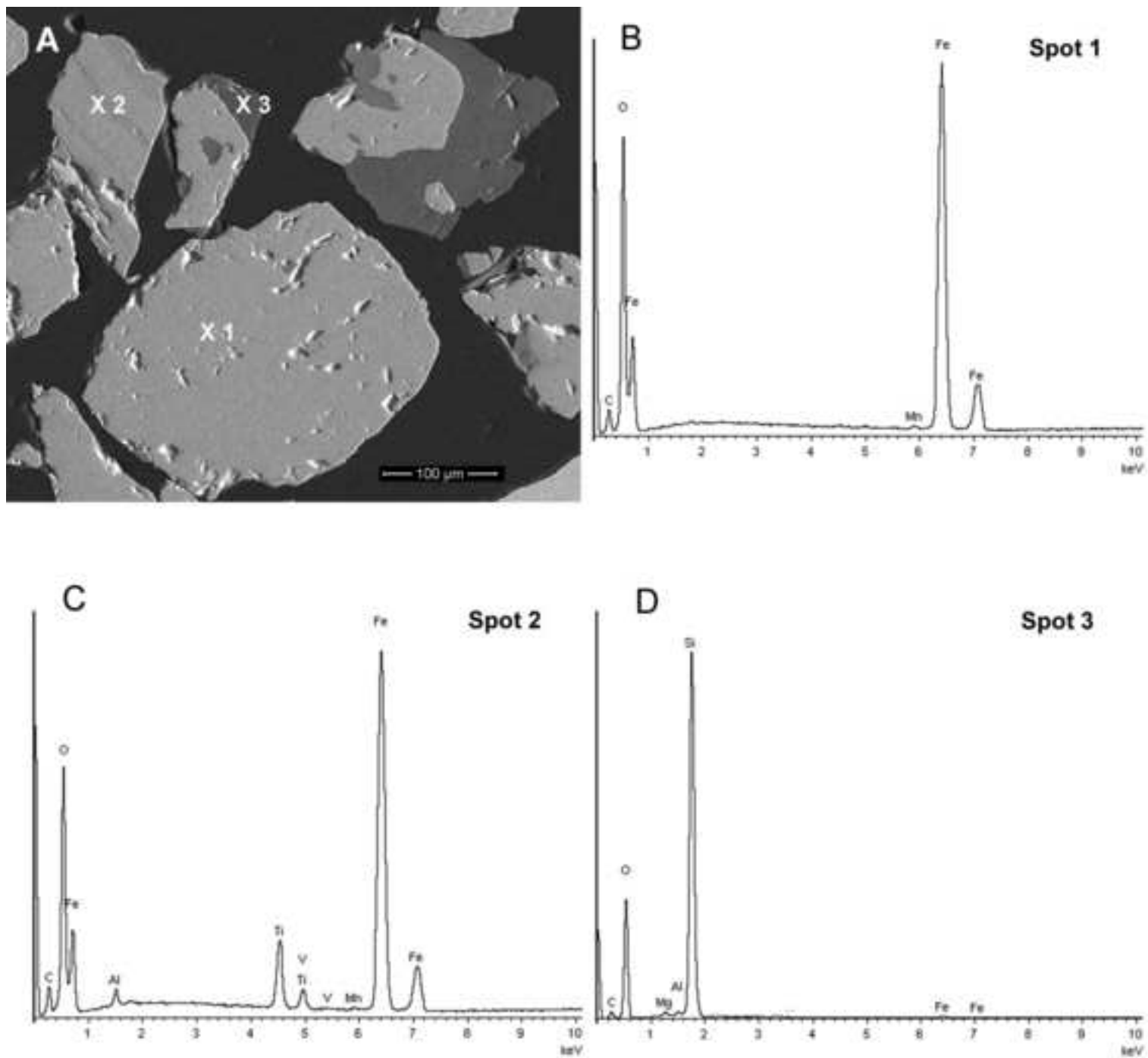
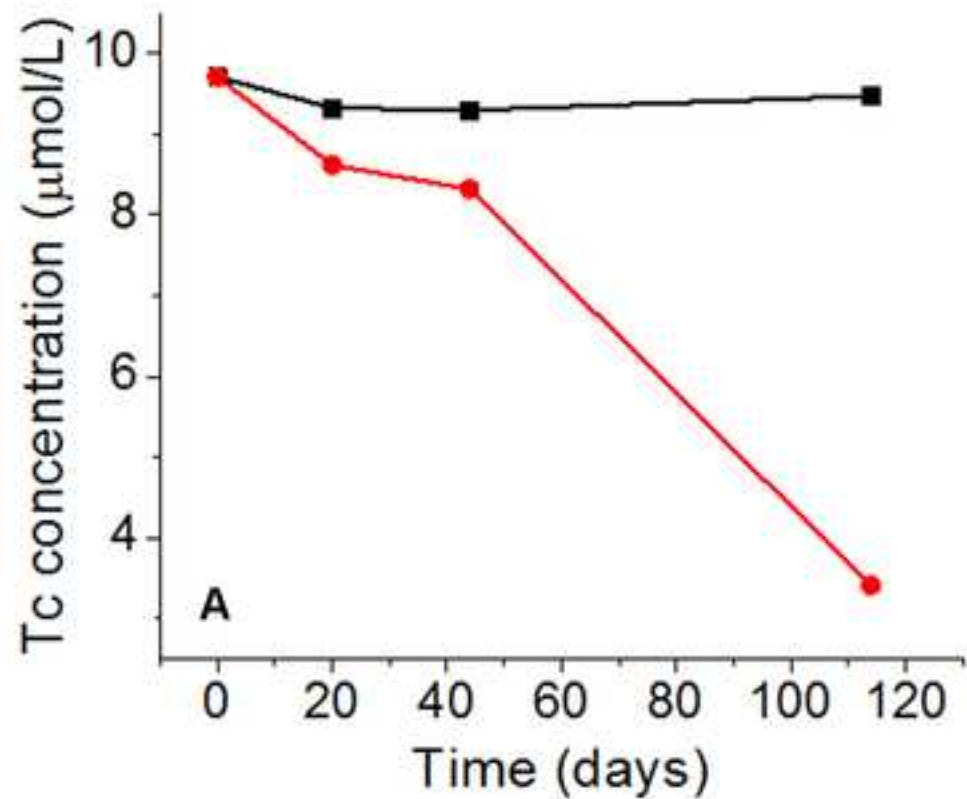**Figure 3**
Click here to download high resolution image
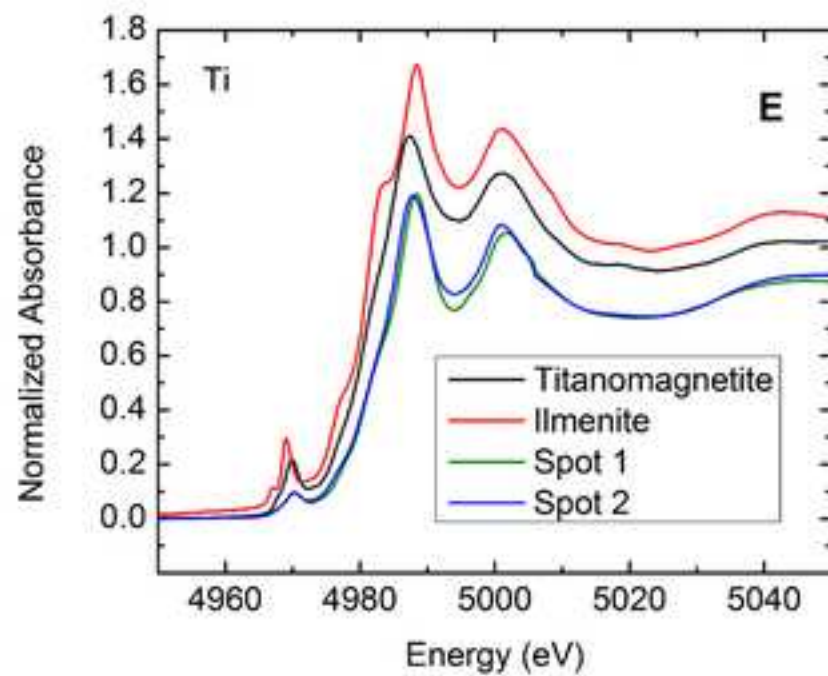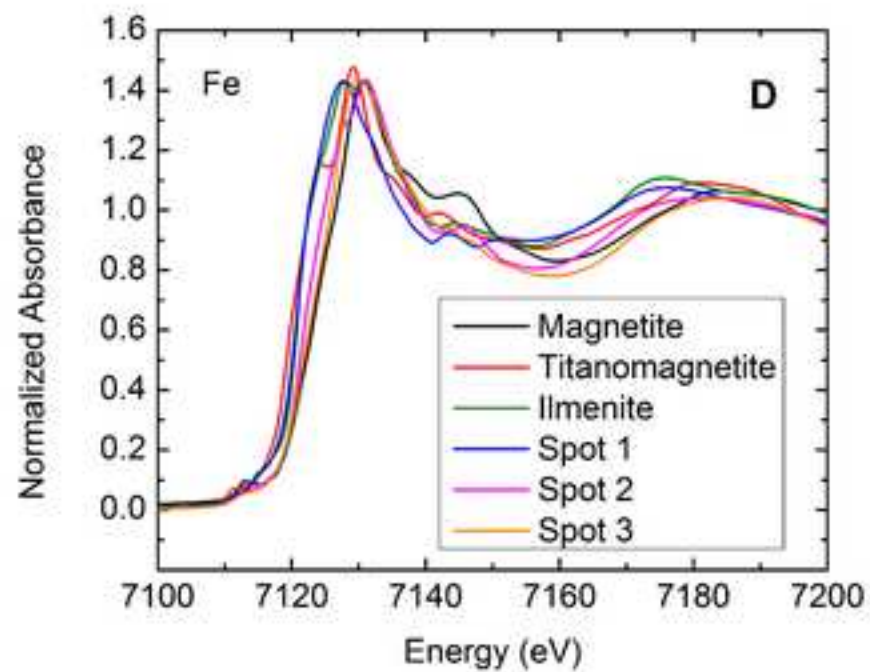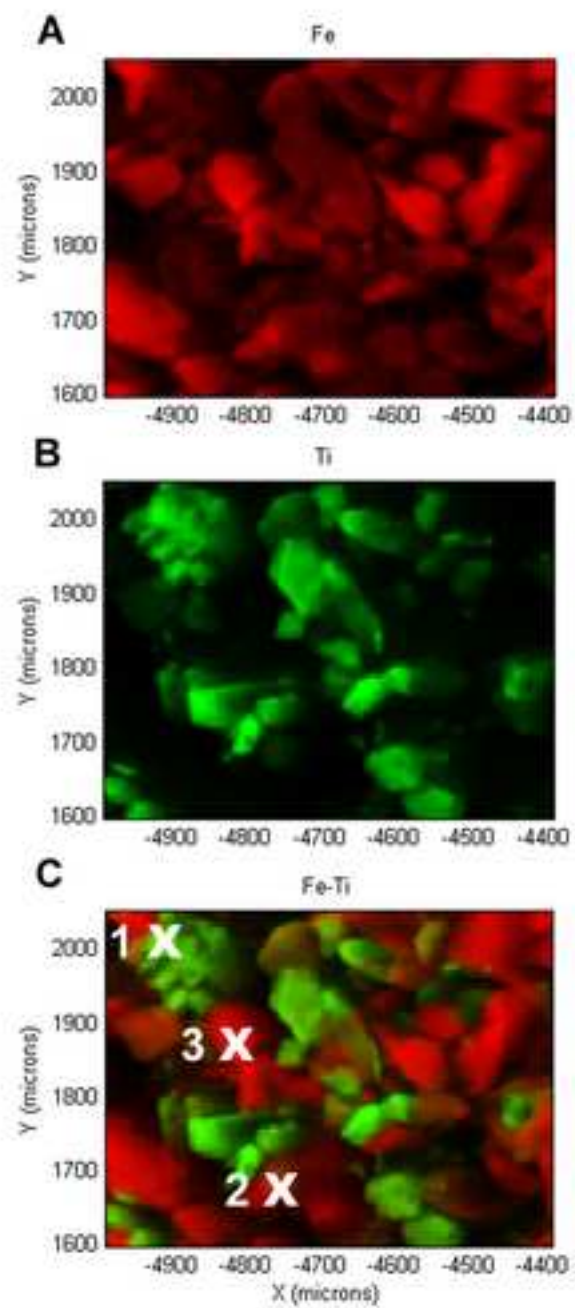
Figure 4
Click here to download high resolution image
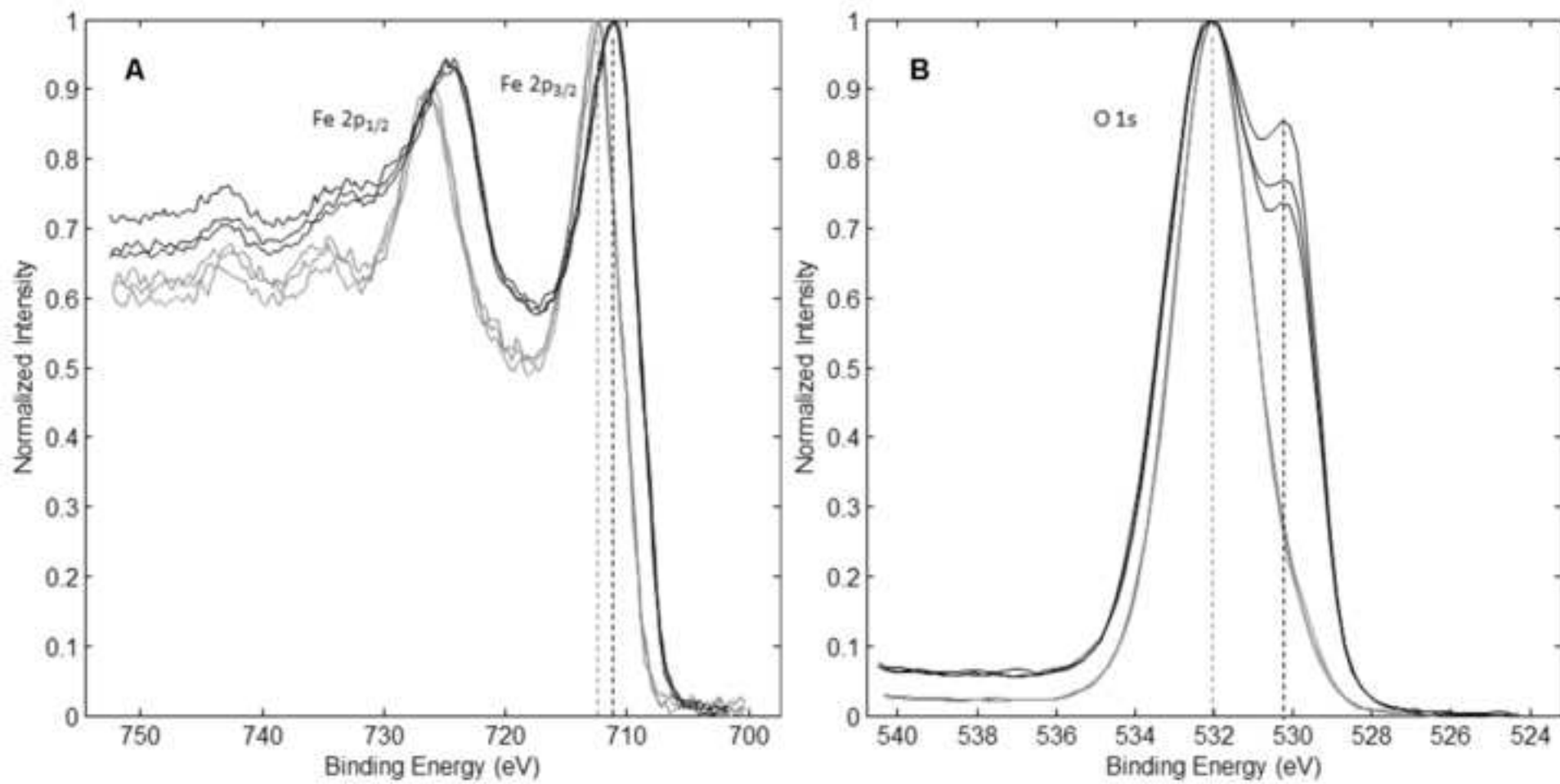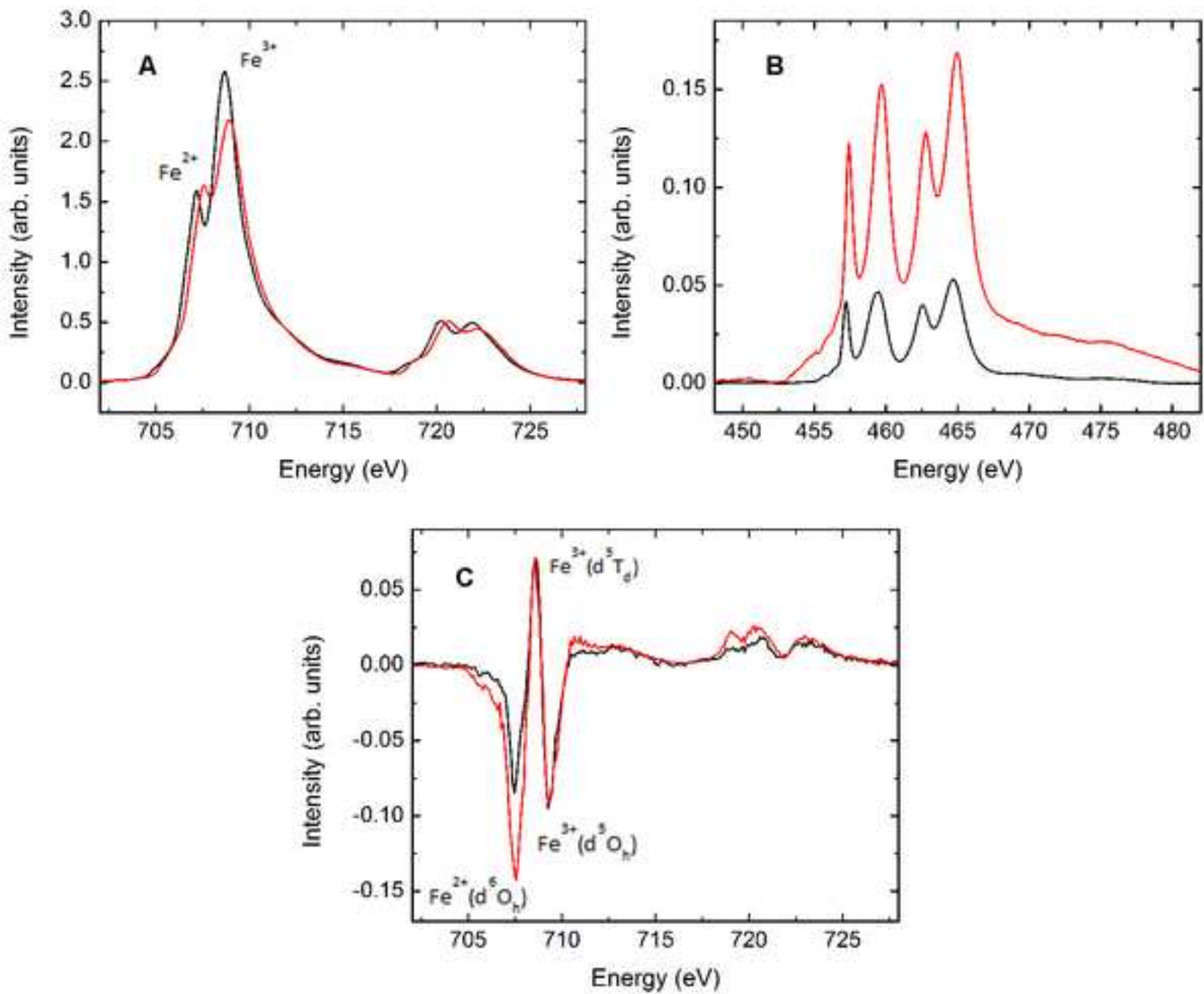
Figure 6
Click here to download high resolution image

Electronic Annex